Composites Science and Technology 168 (2018) 303–311

Contents lists available at ScienceDirect

Composites Science and Technology

journal homepage: www.elsevier.com/locate/compscitech

A novel magnetorheological shear-stiffening elastomer with self-healing ability

Yunpeng Wang[a], Li Ding[a], Chunyu Zhao[a], Sheng Wang[a], Shouhu Xuan[a,**], Han Jiang[b], Xinglong Gong[a,*]

[a] CAS Key Laboratory of Mechanical Behavior and Design of Materials, Department of Modern Mechanics, University of Science and Technology of China (USTC), Hefei 230027, PR China

[b] Applied Mechanics and Structure Safety Key Laboratory of Sichuan Province, School of Mechanics and Engineering, Southwest Jiaotong University, PR China

ARTICLE INFO

Keywords:
Shear-stiffening
Magnetorheological
Self-healing
Constitutive models
Mechanisms

ABSTRACT

A novel magnetorheological shear-stiffening elastomer (MSTE) was prepared by dispersing carbonyl iron particles (CIPs) into the shear-stiffening elastomer, which was synthesized by co-polymerization of shear-stiffening gel (STG) and methyl vinyl silicone rubber (VMQ). The storage modulus of MSTE-80 (the volume ratio of STG and VMQ is 80: 20, and 8.5 vol% carbonyl iron) increased 13100% when the frequency increased from 0.1 Hz to 100 Hz in the oscillation shear measurement. Under applying a magnetic field of 960 mT, the storage modulus of MSTE-80 was further strengthened by 425%. Since the reversible interactions of B—O bonds, the extensibility of the dissected MSTE-60-d recovered to 423% (the initial extensibility ≈ 1050%) after self-healing at 180 °C for 2 h. Meanwhile, constitutive models based on the standard linear solid model were used to describe the shear-stiffening performance and the viscoelastic nature of MSTEs. Finally, possible mechanisms were proposed to explain the shear-stiffening, magnetorheological, and self-healing properties of MSTEs. It was found that the breakage and reconstruction of B—O bonds played a major role in shear-stiffening and self-healing performance. The magnetorheological effects were attributed to the magnetic attraction between the CIPs in the magnetic field.

1. Introduction

Shear-stiffening material is a kind of intelligent materials with prominent rate-dependent rheological and mechanical properties. The common shear-stiffening materials are shear-thickening fluids (STF) and shear-stiffening gel (STG). STF is a type of non-Newtonian fluid that widely exists in concentrated colloidal suspensions [1,2]. The viscosity of STF increases dramatically when the external mechanical stimuli exceed a critical shear rate [2–5]. Because of the reversible shear thickening behavior, STF has attracted considerable interests in soft armor [6], dampers [4,5], impact absorbers [1] and control devices. Nevertheless, as a suspension of particles, STFs meet the problems of sedimentation and volatilization [7]. STG is a lightly cross-linked silicone polymer whose mechanical characters, such as the storage modulus, stiffness, and viscosity increased dramatically when the strain rate increased, and they returned to the original values as soon as the stress was unloaded [8,9]. Comparing to STF, STG is more stable with no sedimentation and volatilization problems. Because of the unique shear-stiffening properties, STG has drawn increasing attention in both fundamental research [10–12] and practical applications in body armor [13,14], shock transmission [15], battery [16], and sensitive sensors [17,18]. STG is a highly viscoelastic material under ambient conditions thus it often exhibits a cold-flow behavior due to the liquid-like nature [19]. Recently, some polymer elastomers which showed similar shear-stiffening performance have been also developed [20,21]. Because of the elastic characteristic, these shear-stiffening elastomers (STE) can recover to its original state after removing the external forces. Good formability of STE will make it a promising material in applications of body armor, impact resistance, and shock transmission. However, the in-depth study on the STE is scarce, and the shear-stiffening performance of the existing STE is not satisfied enough.

In recent years, magnetorheological materials have attracted increasing attention due to their magneto-controllable mechanical properties in the external magnetic fields. One of the most common magnetorheological materials was the magnetorheological elastomer (MRE) composed of magnetic particles and polymer matrixes [22,23]. The

* Corresponding author.
** Corresponding author.
E-mail addresses: xuansh@ustc.edu.cn (S. Xuan), gongxl@ustc.edu.cn (X. Gong).

https://doi.org/10.1016/j.compscitech.2018.10.019
Received 23 April 2018; Received in revised form 7 October 2018; Accepted 15 October 2018
Available online 18 October 2018
0266-3538/

mechanical properties including elastic modulus, storage modulus, and damping could be controlled by the magnetic field [24,25]. Models and theories have been developed to understand the mechanisms and time response of magnetorheological effects of MREs [26,27]. The interfacial interactions of nanoparticles and polymer matrix improved the MR property and reduced the loss factor [27]. Magnetorheological shear-stiffening gels (MSTGs) whose modulus was controlled by the synergistic action of the external stimuli and the magnetic field have been reported [28–30]. Due to the strong interactions between the particles under applying the magnetic field, the mechanical properties of MSTGs were strengthened signally [29]. To further developing the STE, magnetic particles were dispersing into the STE matrix to achieve magneto-controllable mechanical properties.

During the STG preparation, B—O bonds were formed between the polymer chains [18,31,32]. Because of the breakage and reconstruction of B—O bonds, the nanocomposite based on STG showed excellent self-healing ability [17]. The self-healing was achieved through reversible interactions including hydrogen bonding, dynamic borate ester bonding, magnetism, or coordination [33,34]. Self-healing materials were able to repair the mechanical damage automatically and have been studied thoroughly recently [34–37]. Due to the self-healing ability, materials had long service lives and great prospects in the engineering applications [38]. To this end, the new STE prepared by using STG as a raw material would exhibit self-healing properties due to the presence of B—O bonds.

In this work, a novel magnetorheological shear-stiffening elastomer (MSTE) was prepared by dispersing carbonyl iron particles (CIPs) into the STE matrix which was compounded by STG and methyl vinyl silicone rubber. The influencing factors, including volume fraction, strain rate and magnetic field on the mechanical properties of MSTE were studied and analyzed. Self-healing abilities were studied and the temperature effects were discussed. MSTE had larger initial hardness than MSTG and had no cold flow problem. Comparing to traditional STE, MSTE exhibited advantages of magnetic controllability and self-healing ability. Meanwhile, constitutive models and possible mechanisms were proposed to explain the shear-stiffening, magnetorheological, and self-healing properties of MSTEs.

2. Materials and methods

2.1. Preparations

Boric acid (from Sinopharm Chemical Reagent Co. Ltd, Shanghai, China) was mixed with hydroxyl silicone oil (PDMS, 500 mm^2/s, AR degree, from Jining Huakai Resin Co., Ltd) at 50 mg/ml. This mixture was stirred in a ceramic dish at room temperature until homogeneous. Then, the mixture was heated at 180 °C for 2 h and was stirred every 20 min to keep the reaction adequately. During the process, the polymer mixture formed cross-linking, viscous, silky paste. After the paste was cooled to room temperature, the shear-stiffening gel (STG) was obtained.

Next, the STG and the methly vinyl silicone rubber (VMQ 110-2, from Shenzhen Muwei Technology Co., Ltd.) were mixed together in a double-roll mill (Taihu Rubber Machinery Inc., China, Model XK-160). Benzoyl peroxide (BPO, from Sinopharm Chemical Reagent Co. Ltd, Shanghai, China) was added as the vulcanized agent at 4.0 wt% of the rubber mixture. Carbonyl iron particles (CIPs) (Type CN, from BASF, Germany) were also mixed into the mixture at different volume fractions. The diameter of CIPs was about 6μm. The final mixture was pressed into a 1 mm deep aluminum mold and vulcanized at 100 °C, 20 MPa for 15 min. The magnetorheological shear-stiffening elastomer (MSTE) was prepared when the final product cooled down. The schematic of the preparation procedure was shown in Fig. 1. When the volume ratio of STG and VMQ was X: (100-X), the specimen was named as MSTE-X (e.g. MSTE-20 means the volume ratio of STG: VMQ is 20: 80). When the CIPs fraction of MSTE-60s changed, the samples were named as MSTE-60-y (y from a to e). The volume ratios and the CIPs fractions of the samples were listed in Table 1.

2.2. Rheological and tensile tests

Rheological measurements were carried out using an Anton Paar MCR 302 rheometer with a PP20, 20 mm diameter parallel plate geometry (Fig. 2 a, b). All samples were cut into ϕ20 mm × 1 mm coins. By setting the normal force at 1 N, the gap was kept at approximately 1 mm to ensure all the materials were under the same situation during measurements. Prior to tests, the samples were pre-sheared for 1 min at low amplitude (0.1% strain amplitude at 0.1 Hz). Oscillation shear tests were performed at 0.1% strain amplitude. The oscillation shear magnetic sweep tests were done at 0.1% strain amplitude at 1 Hz.

Tensile measurements with low strain were also obtained using the rheometer. The samples were cut into 25 mm × 5 mm rectangular shapes with a thickness of 1 mm. A pair of clamps was designed to clamp 5 mm length at the both ends of the specimens (Fig. 2 c), i.e. the effective tensile lengths of the samples were 15 mm. The clamps and the samples were glued together and reinforced with bolts. Tensile measurements with large strains were performed using a Material Test System (MTS) (MTS criterion 43, MTS System Co., America).

3. Results and discussion

3.1. Rheological properties of MSTEs with different STG volume fractions

First, the rheological properties of MSTE with different volume fractions of STG were studied. The volume fractions of CIPs in MSTEs were maintained at 8.5 vol%. The initial storage moduli (ω= 0.628 rad/s) of MSTE-20 and MSTE-80 were 55.6 kPa, and 3.59 kPa, respectively (Fig. 3 a). When the volume ratio of STG: VMQ increased, the initial storage modulus decreased. Meanwhile, the shear-stiffening performance and the final modulus showed an increasing trend. The relative shear-stiffening performance could be expressed by Ref. [31].

$$RST = \frac{G_f' - G_i'}{G_i'} \times 100\% \quad (1)$$

where G_i' and G_f' are the initial modulus and the final modulus. The results were listed in Table 1. When the volume ratio of STG and VMQ was varied from 0: 100 to 100: 0, the relative shear-stiffening performance increased from 3.23% to 1.25×10^6%. MSTE was synthesized from STG and VMQ. STG is a plastic material with small initial modulus, and vulcanized VMQ is an elastic material with large initial modulus. Therefore, when the STG content increases, MSTE shows more plastic characters and better shear-stiffening performance. Relatively, when the VMQ content increases, MSTE shows elastic properties and the shear-stiffening performance is reduced. Thus, MSTE-0 has the largest initial modulus and MSTE-100 has the best shear-stiffening performance (Fig. 3). In other words, the enhancement of stiffness was based on sacrificing the shear-stiffening performance. The data (Fig. 3 a) was fitted by a hybrid equation S6 (See in Supplementary). The hybrid equation described the storage modulus curves very well.

The rheological properties of the MSTE were affected by the external magnetic field. The storage modulus of MSTEs in the magnetic field of 240 mT were shown in Fig. 3 b. The magnetic field showed a small effect on the modulus of the samples. The initial modulus and the final modulus were a little larger than those without magnetic field. Then, taking the MSTE-60 as an example, the enhancement of the magnetic field on the rheological properties were studied. The storage modulus under applying different magnetic fields were shown in Fig. 3 c. When the magnetic field was increased, both the initial strength and the final strength became larger. The specific relationship between storage modulus and magnetic flux density (B) was shown in Fig. 3 d.

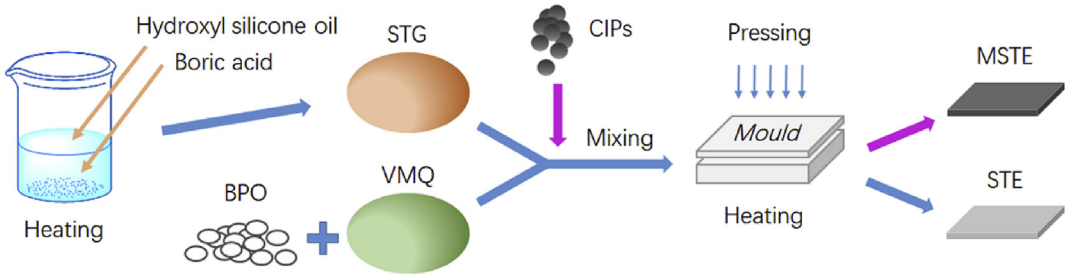

Fig. 1. Schematic diagram of the preparation procedure for MSTE and STE.

Table 1
Volume ratios and CIPs fraction of the samples.

Samples	Volume ratio of STG: VMQ	Volume fraction of CIPs
MSTE-0	0: 100	8.5 vol%
MSTE-20	20: 80	8.5 vol%
MSTE-40	40: 60	8.5 vol%
MSTE-60-a	60: 40	0 vol%
MSTE-60-b	60: 40	3.4 vol%
MSTE-60-c	60: 40	5.6 vol%
MSTE-60-d	60: 40	8.5 vol%
MSTE-60-e	60: 40	12.2 vol%
MSTE-60-f	60: 40	17.2 vol%
MSTE-80	80: 20	8.5 vol%
MSTE-100	100: 0	8.5 vol%

The samples were pre-structured in the 960 mT magnetic field for 3 min before the oscillation shear tests. Moreover, the STG concentration also influenced the mechanical properties. With larger STG volume fraction, the samples had smaller initial moduli and better magnetorheological (MR) effects. The MR effects were attributed to the magnetic attraction between the CIPs in the magnetic field [39]. The relative magnetorheological effects (RME) could be expressed as equation (2) [31].

$$RME = \frac{G'_f - G'_i}{G'_i} \times 100\% \tag{2}$$

The relative shear performance and relative magnetorheological effects results were listed in Table 2.

The cross-link density of the matrix played an important role in the magneto-controllability of MSTE [40]. CIPs in relatively low cross-linked MSTE could be easily moved in the magnetic field to form chain-like microstructures. The chain-like structures could promote the magneto-induced storage modulus. In the preparation of MSTE, the cross-links were mainly formed by the VMQ and BPO. Thus, MSTE with larger STG volume fraction showed higher magnetorheological performance.

To further comprehend the viscoelastic mechanical characters of MSTE, the creep behaviors were studied under a constant stress of 50 Pa, and the curves were plotted in Fig. 4 a. The viscous flow strain was produced in the secondary creep, which was an irreversible component of strain [41]. After unloading, the maximum strain of MSTE-0 and MSTE-20 was merely 0.075% and returned to zero. In the recovery section, the unrecoverable strain of MSTEs increased while the volume fraction of STG increased. However, MSTE-100 could hardly recover from the 78.1% plastic strain thus showed the cold flow phenomenon. The pictures of MSTE samples demonstrated that the cold flow only occurred in MSTE-100 (Fig. 4 b).

The creep results were fitted to equations S6 and S8 (in Supplementary) (the blue imaginary lines in Fig. 4 a). The SLS model described the first creep section well, while it failed in the recovery section. Then, the SLS model was optimized to SLSX model (Fig. S3 in Supplementary). As shown the black solid lines in Fig. 4 a, the SLSX model agreed well with the creep behavior results. The fitting correlation coefficients of SLSX model was much higher than the SLS model.

Tensile measurements and steady shear tests were carried out to further study the rate-dependent viscoelastic properties of MSTEs. The MSTE-60-d was chosen as the samples. As the strain rate increased, the modulus obviously increased, indicating the typical rate-dependent mechanical property (Fig. 5). When the shear rate changed from 0.004 s^{-1} to 0.1 s^{-1}, the shear modulus of MSTE-60-d increased from 43 to 343 kPa. The rate-dependent mechanical properties were attributed to the breakage and reconstruction of B—O bonds during the deformation, which would be discussed in the following section. The results were fitted to the SLS model and were well described (solid lines in Fig. 5). The SLS model was sufficient to describe the stress-strain curves of MSTE-60-d.

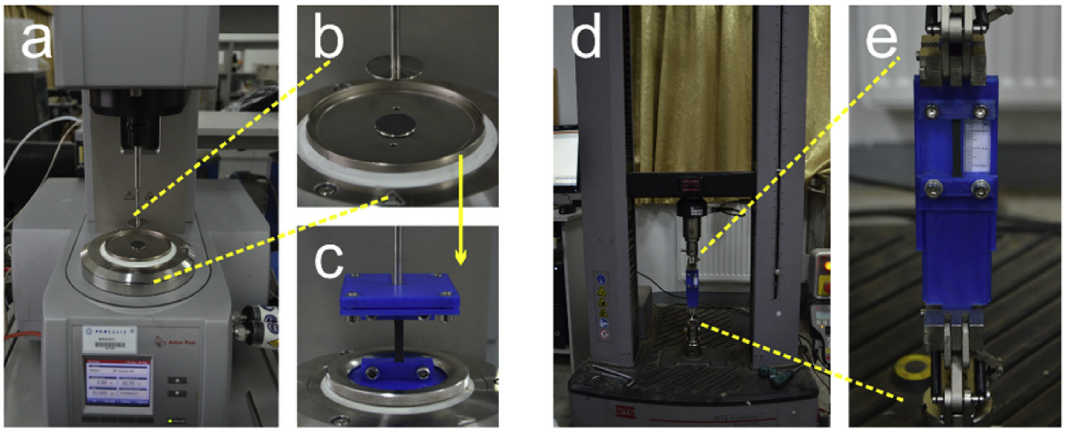

Fig. 2. Rheological and tensile measure systems. (a), (b), and (c) The MCR 302 rheometer, the PP20 parallel plate, and the tensile fixture. (d), (e) The Material Test System and the matched tensile fixture. The fixtures in (c) and (e) were made out of PLA plastic by 3D printing.

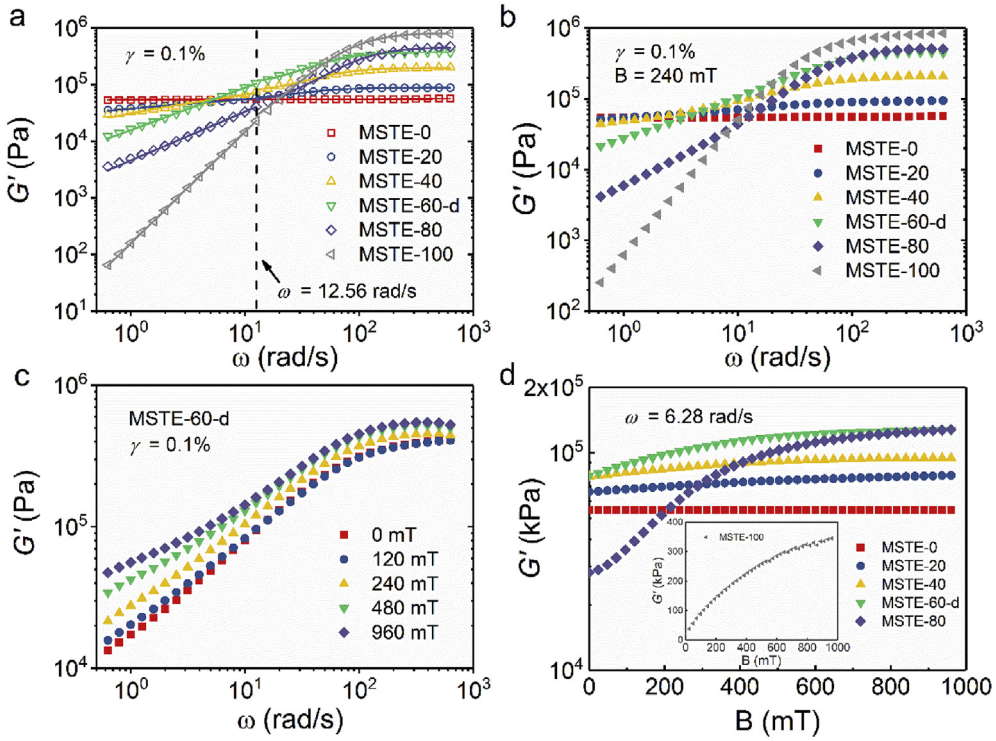

Fig. 3. Rheological properties of MSTEs. (a) Storage modulus (G') in oscillation shear tests. Solid lines are fits to equation S6. (b) G' of MSTEs in the 240 mT magnetic field. (c) G' of MSTE-60-d in different magnetic fields. (d) G' as a function of B. The insert was the results for MSTE-100.

3.2. Mechanical properties of MSTE-60-d with different CIPs volume fractions

Next, the mechanical properties MSTE-60 with different CIPs volume fractions were investigated. Rheological measurements were shown in Fig. 6. The storage moduli increased with increasing angular frequency, demonstrating the shear-stiffening performance (Fig. 6 a). The presence of CIPs in MSTE-60 promoted the initial moduli and reduced the shear-stiffening performance. When the volume fraction of CIPs changed from 0 to 17.2 vol%, the relative shear-stiffening performance decreased from 5190% to 1650%. CIPs occupied the intermolecular gaps and hindered the movement of the MSTE molecules. This led to a reduction in the relative shear-stiffening performance.

The oscillation shear tests were carried out under applying the magnetic field (Fig. 6 b). Comparing the results of Fig. 6 a and b, the storage modulus in the magnetic field was larger. The maximum storage modulus of MSTE-60-e was 0.29 MPa and 0.71 MPa in the magnetic field of 0 and 240 mT, respectively. The magnetic field showed no effect on the MSTE-60-a. That the curves of MSTE-60-b showed drops at last was because of the slipping between the rheometer rotor and the samples. Then, the oscillation shear tests were performed in an increasing magnetic field to study the magneto-induced storage modulus (Fig. 6 c). Obviously, the magnetic field exhibited a larger effect on the storage modulus of samples with larger volume fractions. The relationship between the storage modulus G' and the magnetic flux density B was deemed as following.

$$G' - G_0 = \lambda B = \Delta G \tag{3}$$

where G_0 is the initial storage modulus, ΔG is the magneto-induced storage modulus, and λ is a constant related to the volume fraction of CIPs. The experimental results were well described by equation (3). As reported in previous work [42,43], the relation between ΔG and the volume fraction of CIPs ϕ was a quadratic function.

$$\lambda = a\phi^2 \tag{4}$$

where a was a constant coefficient. The fitting results gave $a = 0.73\ kPa{\cdot}T^{-1}$ (Fig. 6 d). Thus, ΔG of MSTE could be expressed as the following equation.

$$\Delta G = a\phi^2 B = 0.73\phi^2 B \tag{5}$$

The experimental results and equation (5) demonstrated that the MSTE showed a good magneto-controllable mechanical property. By changing the magnetic field, mechanical properties of MSTE could be adjusted to the specific application situations.

3.3. Self-healing performance of MSTE

The B—O bonds formed between the polymer chains of MSTE could break and reform during the deformation, resulting in good self-healing properties [29,31]. Tensile tests were performed to study the self-healing properties of MSTE with different STG volume fractions. Samples (25 mm × 5mm × 1 mm) were cut in half and spliced in the healing measurements. The effective tensile length was $L_0 = 15\ mm$, and the tensile velocity was $dL/dt = 500\ \mu m/s$. Thus, the tensile strain rate was 0.033 s^{-1}. Tensile stress-strain curves for original MSTE-0, MSTE-20, MSTE-40 and MSTE-60-d were plotted in Fig. 7 a. The results

Table 2
Relative shear-stiffening performance (RST) and relative magnetorheological effects (RME) of MSTE.

	MSTE-0	MSTE-20	MSTE-40	MSTE-60-d	MSTE-80	MSTE-100
RST (%)	5.93	14.8	580	2.92×10^3	1.31×10^4	1.25×10^6
RME (%)	0	18.9	21.6	62.0	355	1520

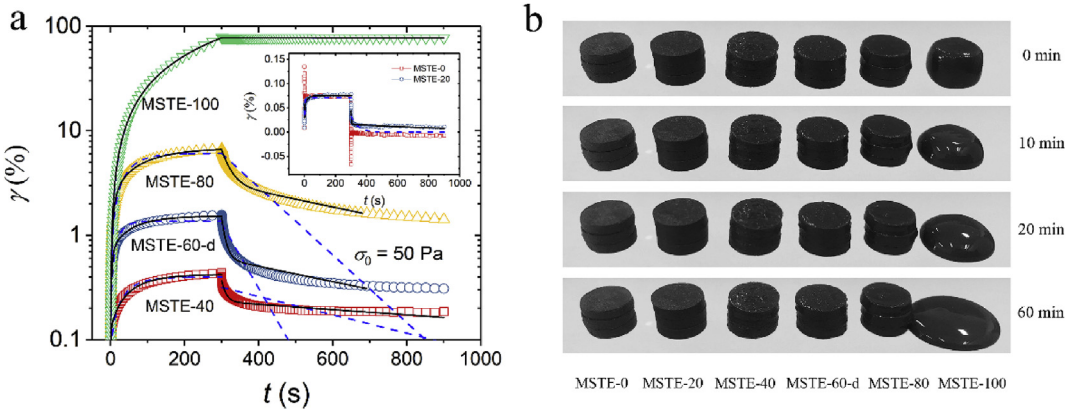

Fig. 4. Creep behaviors of MSTE. (a) Strain curves of MSTEs in the creep measurements with 50 Pa constant stress. Insert graph is the curves of MSTE-0 and MSTE-20. The blue imaginary lines are fits to the SLS model. The black solid lines are fits to the SLSX model. (b) Cold flow phenomena of MSTE samples. (For interpretation of the references to colour in this figure legend, the reader is referred to the Web version of this article.)

were well described by the SLS model (black solid lines in Fig. 7 a). The areas enveloped by tensile hysteresis curves showed the viscoelastic nature of MSTE were deemed as the absorbed energy. MSTE-0 sample broke at about 110% strain, and did not show self-healing ability in the experiments. Tensile stress-strain curves for self-healing MSTE-20, MSTE-40 and MSTE-60-d samples were plotted in Fig. 7 b. With smaller volume fraction of STG, MSTE had larger elastic modulus manifesting as steeper increasing trends of the tensile stress and had better healing performance showing as larger extensibility.

Then, the spliced samples were heated at 100 °C (the vulcanization temperature) for 2 h. The thermal-healing curves were compared with 3 min self-healing curves (Fig. 7 b). The healing performance was improved by about 30%. In addition, by comparing the stress-strain curves (Fig. 7 b) and the fitting lines in Fig. 7 a, the healing samples showed virtually the same mechanical behaviors as the original samples within the fracture strains. Spontaneously, the healing performance of samples with longer time and higher temperature were studied (Fig. 7 c). The healing time had a little effect on the self-healing performance, and the temperature played an important role in thermal-healing performance. After thermal-healing at 180 °C for 2 h, MSTE-60-d recovered to 423% extensibility. When MSTE samples were heated at 180 °C (the fabrication temperature of STG), the fracture edges approached melting, and B and O atoms could fully contact and form B—O bonds to repair the broken materials.

Besides, the self-healing properties were also studied with oscillation shear tests (Fig. 7 d). A 1 mm thick sample of MSTE-60-d was cut into four pieces and spliced together. Two 1 mm thick samples were superimposed into a 2 mm thick sample. The oscillation shear curves of the four samples were almost identical, demonstrating the self-healing properties of MSTE-60-d.

Finally, the self-healing properties of MSTE-60-d samples with different CIPs fractions were studied. The tensile breaking strains of original samples were shown in Fig. 8 a. When the CIPs fraction increased, the breaking strain almost unchanged. The extensibilities were about 1050%. The breaking strains of samples after 3 min self-healing were plotted in Fig. 8 b. All the samples with different CIPs showed similar self-healing properties while the healed extensibilities were about 90%. The minor difference between the samples was attributed to the accidental error during the preparation procedure. It could be concluded that the CIPs fraction had little effect on the self-healing properties.

4. Mechanisms

4.1. Mechanisms of MSTEs' shear-stiffening performance

The ATR-FITR spectroscopy demonstrated that the Si—O—Si bonds constituted the polymer chains of MSTE (Fig. S1 in Supplementary). Therefore, the backbone of MSTE was shown in Fig. 9 c [31]. Boric acid was added to the formulation to introduce boron into the MSTE molecule. As reported by Houston [32], the electron-deficient p orbital of the B atom could obtain electrons from the O in the Si—O structure (Fig. S1 in Supplementary) to form B—O bonds (Fig. 9 c). The B—O bond was a reversible interaction which could self-reforming after breaking [31].

When low-rate shear was applied, MSTE slightly deformed and the molecule chains gradually moved. A small amount of B—O bonds provided some resistance to shearing motion. Comparing to the damping

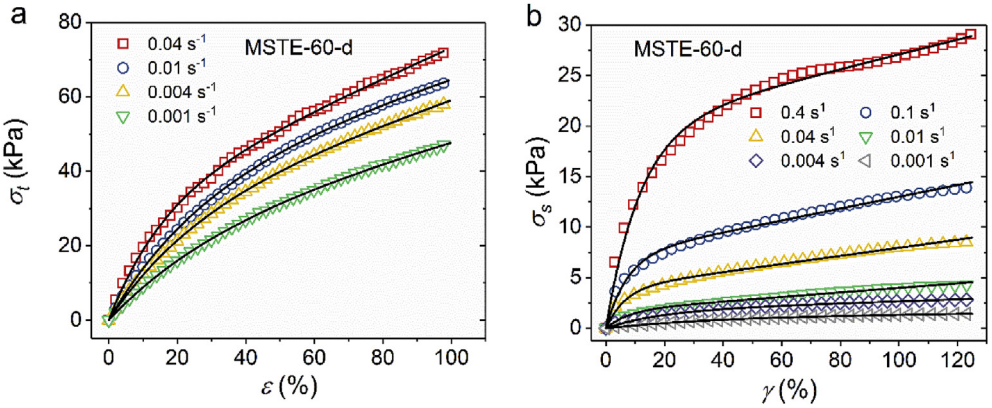

Fig. 5. Rate-dependent properties of MSTE-60-d. (a) Tensile stress-strain curves with different strain rates. The black solid lines are fits to equation S2. (b) Steady shear stress-strain curves with different shear rates. The black solid lines are fits to equation S3.

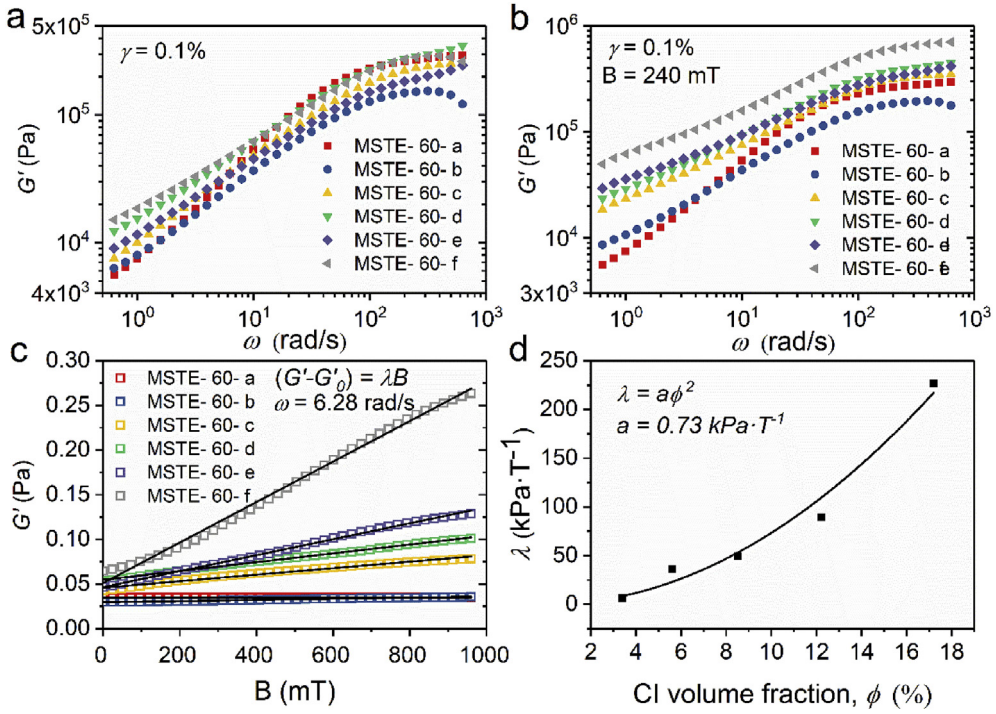

Fig. 6. Rheological properties of MSTE-60. (a) Frequency sweeping curves at 0.1% strain amplitude. (b) Frequency sweeping results in the magnetic field of 240 m T. (c) G' as a function of B. The solid lines are fits to equation (3). (d) The relationship between the fit parameter λ and the volume fraction ϕ.

force of the matrix, the disruptive force of B—O bonds was much smaller. The storage modulus of MSTE mainly depended on the matrix. As the shear rate increased, the MSTE molecule chains moved rapidly. Large amounts of B—O bonds took action to resist the deformation of MSTE. The effective B—O bonds were broken quickly and the active B and O atoms reformed B—O bonds again. The disruptive force of B—O bonds grew to be larger than the matrix's damping force, leading to the sharp increment of the storage modulus. After the stress was unloaded, the deformation of MSTE gradually recovered due to the elasticity of the matrix. The mechanical properties returned to the original state in the meantime.

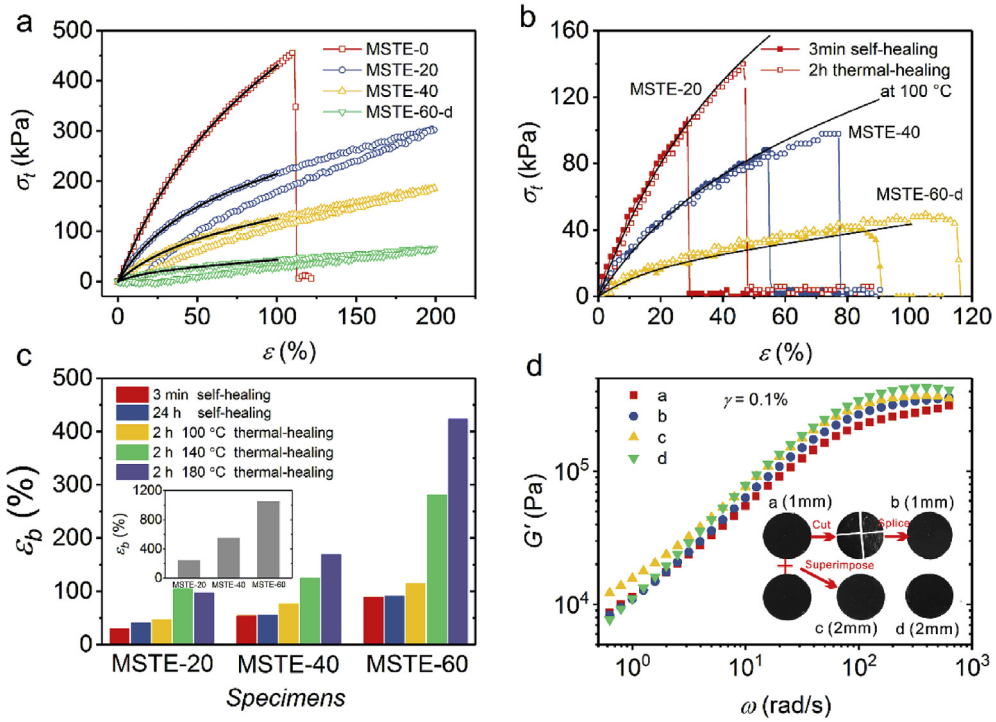

Fig. 7. Self-healing and thermal-healing properties of MSTE. (a) Tensile stress-strain curves at 0.033 s^{-1}. The solid lines are fits to the SLS model. (b) Tensile stress strain curves after cutting and healing. The solid lines are fitting lines in figure a. (c) Breaking strains ε_b of healing samples with different conditions. Insert graph is the breaking strain of original samples. (d) Oscillation shear results of original samples and healing samples.

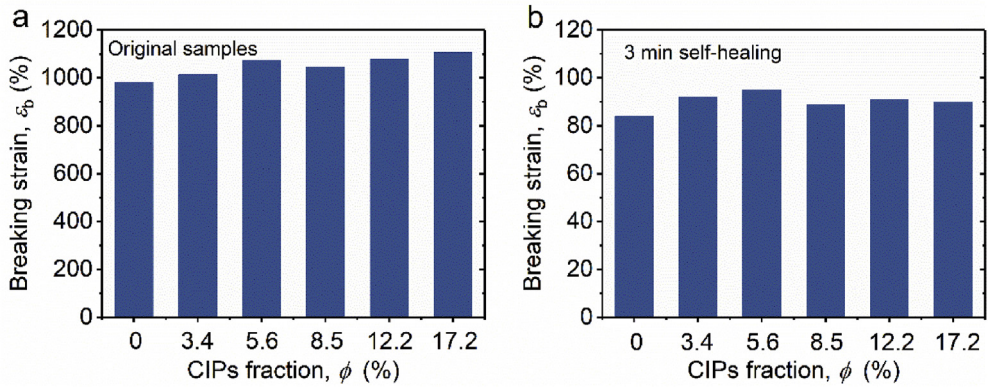

Fig. 8. Self-healing properties of MSTE-60-d samples with different CIPs fractions. (a) and (b) are the breaking strains of original samples and samples after 3 min self-healing, respectively.

4.2. Mechanisms of the magneto-controllable mechanical properties of MSTEs

It was known that the aggregation of nanoparticles reduced the creep resistance of nanocomposite [44]. The creep resistance had an important effect on the construction of chain-like microstructures, which induced the MR effect [40]. At normal state, CIPs were evenly distributed in the cross-linking matrix (Fig. 9 a). In shearing, the CIPs increased the friction force between the molecule chains. Therefore, the greater volume fraction, the greater initial storage modulus of MSTE. Magnetized CIPs could be modelled as magnetic dipole moments, when an external magnetic field was applied [42]. The magnetic dipole moment $\vec{m}_j$ was respectively subjected to the attractive force F_{ij} and F_{kj} from the magnetic dipole moments $\vec{m}_i$ and $\vec{m}_k$ (Fig. 9 a). At the same time, the attractive force F_{ji} and F_{jk} traced back to $\vec{m}_i$ and $\vec{m}_k$. The attractive force between the magnetic dipoles tended to align the CIPs to form chain-like microstructures with the external applied magnetic field, leading to the magnetostriction of the MSTE [45,46].

When the shear stress was applied to the MSTE, the distance between the CIPs increased. The magnetic-attractive force between the CIPs resisted the shearing motion and hindered the deformation of the matrix. The increase of the resistance of deformation further increased the storage modulus of MSTE. The larger the volume fraction, the smaller the average distance between the CIPs. The relationship

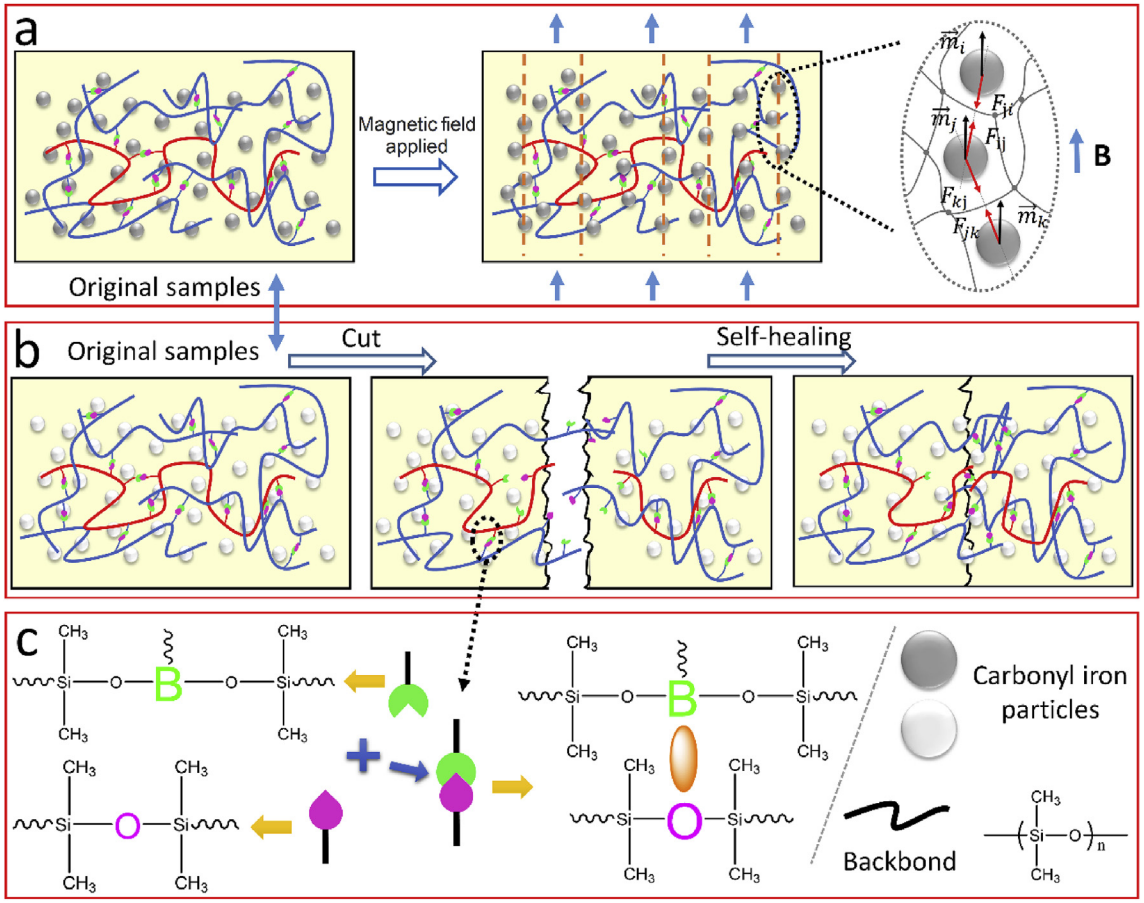

Fig. 9. The mechanism schematic diagrams of MSTE and chemical structures of the B-O bonds. (a) Mechanism diagrams of the magneto-controllable mechanical properties. (b) Mechanisms of self-healing properties. (c) Chemical structures of B-O bonds and the backbond.

between the magneto-induced storage modulus and the volume fraction was a quadratic equation [42,43].

4.3. Mechanisms of the self-healing properties of MSTEs

B—O bonds connected the long molecular chains together to reinforce the cross-linking structure in MSTE samples (Fig. 9 c). When the MSTE was cut in half, some B—O bonds and molecular chains were broken (Fig. 9 b). The two parts of the sample were then brought into contact and laid aside for about 5 min. The active B and O atoms at the interface contacted and reformed B—O bonds. The molecule chains were bound and the dissected sample was self-healed. When the samples were heated, the B and O atoms became more active and the healing performance was promoted consequently.

5. Conclusion

In conclusion, a new magnetorheological shear-stiffening elastomer (MSTE) was synthesized from STG, VMQ and CIPs. The mechanical properties of MSTE were highly dependent on the strain rate and could be controlled by the magnetic field. In the oscillation shear measurement, the storage modulus of MSTE-80 showed a maximum increase of 13100% when the frequency increased from 0.1 Hz to 100 Hz, indicating the excellent shear-stiffening performance. When a magnetic field of 960 mT was applied to the MSTE-80, the storage modulus was strengthened by 425%, showing the magnetic controllability. The relation between the magnetic field, the magneto-induced modulus, and the volume fraction of CIPs was expressed as an equation that was consistent with the experimental results. In addition, due to the reversible interaction of B—O bonds, MSTE exhibited a good self-healing ability that the dissected MSTE-60-d recovered to an extensibility of 423% after healing. Meanwhile, constitutive models based on the standard linear solid model were used to describe the mechanical properties of MSTEs. All the experimental results agreed well with the constitutive models. Possible mechanisms were proposed based on the experimental results. The breakage and reconstruction of B—O bonds played a major role in shear-stiffening and self-healing performance. The magnetorheological effects were attributed to the magnetic attraction between the CIPs in the magnetic field. The unique properties of MSTE will make it a promising material for applications in body armors, and impact resistance, etc.

Acknowledgements

Financial support from the National Natural Science Foundation of China (Grant No. 11772320, 11572309), the Strategic Priority Research Program of the Chinese Academy of Sciences (Grant No. XDB22040502), and the Opening Project of Applied Mechanics and Structure Safety Key Laboratory of Sichuan Province (SZDKF-1701) is gratefully acknowledged. This study was also supported by the Collaborative Innovation Center of Suzhou Nano Science and Technology.

Appendix A. Supplementary data

Supplementary data to this article can be found online at https://doi.org/10.1016/j.compscitech.2018.10.019.

References

[1] H. Zhang, X. Zhang, Q. Chen, X. Li, P. Wang, E.H. Yang, F. Duan, X. Gong, Z. Zhang, J. Yang, Encapsulation of shear thickening fluid as an easy-to-apply impact-resistant material, J. Mater. Chem. A 5 (43) (2017) 22472–22479.
[2] Q. Chen, S.H. Xuan, W.Q. Jiang, S.S. Cao, X.L. Gong, Shear time dependent viscosity of polystyrene-ethylacrylate based shear thickening fluid, Smart Mater. Struct. 25 (4) (2016).
[3] X. Gong, Q. Chen, M. Liu, S. Cao, S. Xuan, W. Jiang, Squeeze flow behavior of shear thickening fluid under constant volume, Smart Mater. Struct. 26 (6) (2017) 065017.
[4] H. Zhou, L. Yan, W. Jiang, S. Xuan, X. Gong, Shear thickening fluid-based energy-free damper: design and dynamic characteristics, J. Intell. Mater. Syst. Struct. 27 (2) (2016) 208–220.
[5] X.Z. Zhang, W.H. Li, X.L. Gong, The rheology of shear thickening fluid (STF) and the dynamic performance of an STF-filled damper, Smart Mater. Struct. 17 (3) (2008) 035027.
[6] S.S. Cao, Q. Chen, Y.P. Wang, S.H. Xuan, W.Q. Jiang, X.L. Gong, High strain-rate dynamic mechanical properties of Kevlar fabrics impregnated with shear thickening fluid, Compos. Part. A Appl. Sci. Manuf. 100 (2017) 161–169.
[7] E. Brown, H.M. Jaeger, The role of dilation and confining stresses in shear thickening of dense suspensions, J. Rheol. 56 (4) (2012) 875–923.
[8] R. Bandyopadhyay, Novel experimentally observed phenomena in soft matter, Pramana 81 (1) (2013) 3–34.
[9] R. Cross, Elastic properties of plasticine, Silly Putty, and tennis strings, Phys. Teach. 50 (9) (2012) 527.
[10] J. Koser, Laboratory activity: specific heat by change in internal energy of Silly Putty, Phys. Teach. 49 (9) (2011) 574.
[11] O. Kulikov, K. Hornung, Novel processing aid based on modified Silly Putty®, J. Vinyl Addit. Technol. 12 (3) (2006) 131–142.
[12] Z. Liu, S.J. Picken, N.A.M. Besseling, Polyborosiloxanes (PBSs), synthetic kinetics, and characterization, Macromolecules 47 (14) (2014) 4531–4537.
[13] C. Xu, Y. Wang, J. Wu, S. Song, S. Cao, S. Xuan, W. Jiang, X. Gong, Anti-impact response of Kevlar sandwich structure with silly putty core, Compos. Sci. Technol. 153 (2017) 168–177.
[14] Q. He, S. Cao, Y. Wang, S. Xuan, P. Wang, X. Gong, Impact resistance of shear thickening fluid/Kevlar composite treated with shear-stiffening gel, Compos. Part. A Appl. Sci. Manuf. 106 (2018) 82–90.
[15] J. Liang, X.H. Zhang, Rheological properties of SP in shock transmission application, J. Mater. Civ. Eng. 27 (9) (2014) 04014250.
[16] K. Liu, A. Pei, H.R. Lee, B. Kong, N. Liu, D. Lin, Y. Liu, C. Liu, P.c. Hsu, Z. Bao, Y. Cui, Lithium metal anodes with an adaptive "Solid-Liquid" interfacial protective layer, J. Am. Chem. Soc. 139 (13) (2017) 4815–4820.
[17] S. Wang, S. Xuan, W. Jiang, W. Jiang, L. Yan, Y. Mao, M. Liu, X. Gong, Rate-dependent and self-healing conductive shear stiffening nanocomposite: a novel safeguarding material with force sensitivity, J. Mater. Chem. A 3 (39) (2015) 19790–19799.
[18] C.S. Boland, U. Khan, G. Ryan, S. Barwich, R. Charifou, A. Harvey, C. Backes, Z. Li, M.S. Ferreira, M.E. Mobius, R.J. Young, J.N. Coleman, Sensitive electromechanical sensors using viscoelastic graphene-polymer nanocomposites, Science 354 (6317) (2016) 1257–1260.
[19] S. Wang, S. Xuan, Y. Wang, C. Xu, Y. Mao, M. Liu, L. Bai, W. Jiang, X. Gong, Stretchable polyurethane sponge scaffold strengthened shear stiffening polymer and its enhanced safeguarding performance, ACS Appl. Mater. Interfaces 8 (7) (2016) 4946–4954.
[20] R. Martin, A. Rekondo, A. Ruiz de Luzuriaga, A. Santamaria, I. Odriozola, Mixing the immiscible: blends of dynamic polymer networks, RSC Adv. 5 (23) (2015) 17514–17518.
[21] T. Tian, W. Li, J. Ding, G. Alici, H. Du, Study of shear-stiffened elastomers, Smart Mater. Struct. 21 (12) (2012) 125009.
[22] G. Peng, Y. Ge, J. Ding, C. Wang, G.G. Wallace, W. Li, Magnetorheological technology for fabricating tunable solid electrolyte with enhanced conductivity and mechanical property, Smart Mater. Struct. 27 (3) (2018) 035022.
[23] S.A.A. Aziz, S.A. Mazlan, N.I.N. Ismail, S.B. Choi, Ubaidillah, N.A.B. Yunus, An enhancement of mechanical and rheological properties of magnetorheological elastomer with multiwall carbon nanotubes, J. Intell. Mater. Syst. Struct. 28 (20) (2017) 3127–3138.
[24] S. Sun, J. Yang, T. Yildirim, H. Du, G. Alici, S. Zhang, W. Li, Development of a nonlinear adaptive absorber based on magnetorheological elastomer, J. Intell. Mater. Syst. Struct. 29 (2) (2017) 194–204.
[25] S. Sun, J. Yang, H. Du, W. Li, Overcoming the conflict requirement between high-speed stability and curving trafficability of the train using an innovative magnetorheological elastomer rubber joint, J. Intell. Mater. Syst. Struct. 29 (2) (2017) 214–222.
[26] M. Zhu, M. Yu, S. Qi, J. Fu, Investigations on response time of magnetorheological elastomer under compression mode, Smart Mater. Struct. 27 (5) (2018) 055017.
[27] M. Yu, S. Qi, J. Fu, M. Zhu, D. Chen, Understanding the reinforcing behaviors of polyaniline-modified carbonyl iron particles in magnetorheological elastomer based on polyurethane/epoxy resin IPNs matrix, Compos. Sci. Technol. 139 (2017) 36–46.
[28] N. Golinelli, A. Spaggiari, E. Dragoni, Mechanical behaviour of magnetic Silly Putty: viscoelastic and magnetorheological properties, J. Intell. Mater. Syst. Struct. 28 (8) (2017) 953–960.
[29] Y. Wang, S. Wang, C. Xu, S. Xuan, W. Jiang, X. Gong, Dynamic behavior of magnetically responsive shear-stiffening gel under high strain rate, Compos. Sci. Technol. 127 (2016) 169–176.
[30] F. Guo, C.B. Du, G.J. Yu, R.P. Li, The static and dynamic mechanical properties of magnetorheological Silly Putty, Adv. Mater. Sci. Eng. 2016 (2016) 1–11.
[31] S. Wang, W. Jiang, W. Jiang, F. Ye, Y. Mao, S. Xuan, X. Gong, Multifunctional polymer composite with excellent shear stiffening performance and magnetorheological effect, J. Mater. Chem. C 2 (34) (2014) 7133.
[32] M.P. Goertz, X.Y. Zhu, J.E. Houston, Temperature dependent relaxation of a "solid-liquid", J. Polym. Sci., Part B: Polym. Phys. 47 (13) (2009) 1285–1290.
[33] Z. Wang, Q. Pan, An omni-healable supercapacitor integrated in dynamically cross-linked polymer networks, Adv. Funct. Mater. 27 (24) (2017) 1700690.
[34] J. Wu, L.H. Cai, D.A. Weitz, Tough self-healing elastomers by molecular enforced integration of covalent and reversible networks, Adv. Mater. 29 (38) (2017).

[35] Z. Wang, F. Tao, Q. Pan, A self-healable polyvinyl alcohol-based hydrogel electrolyte for smart electrochemical capacitors, J. Mater. Chem. A 4 (45) (2016) 17732–17739.
[36] I.L. Hia, V. Vahedi, P. Pasbakhsh, Self-healing polymer composites: prospects, challenges, and applications, Polym. Rev. 56 (2) (2016) 225–261.
[37] Y. Guo, X. Zhou, Q. Tang, H. Bao, G. Wang, P. Saha, A self-healable and easily recyclable supramolecular hydrogel electrolyte for flexible supercapacitors, J. Mater. Chem. A 4 (22) (2016) 8769–8776.
[38] v.d.Z.P.D. Sybrand, Self Healing Materials, Springer, Netherlands, 2007.
[39] S.Y. Tang, X. Zhang, S. Sun, D. Yuan, Q. Zhao, S. Yan, L. Deng, G. Yun, J. Zhang, S. Zhang, Versatile microfluidic platforms enabled by novel magnetorheological elastomer microactuators, Adv. Funct. Mater. 28 (8) (2018) 1705484.
[40] Y. Fan, X. Gong, S. Xuan, L. Qin, X. Li, Effect of cross-link density of the matrix on the damping properties of magnetorheological elastomers, Ind. Eng. Chem. Res. 52 (2) (2012) 771–778.
[41] S. Qi, M. Yu, J. Fu, P.D. Li, M. Zhu, Creep and recovery behaviors of magnetorheological elastomer based on polyurethane/epoxy resin IPNs matrix, Smart Mater. Struct. 25 (1) (2016).
[42] M.R. Jolly, J.D. Carlson, B.C. Munoz, A model of the behaviour of magnetorheological materials, Smart Mater. Struct. 5 (5) (1996) 607.
[43] J. Yang, X. Gong, H. Deng, L. Qin, S. Xuan, Investigation on the mechanism of damping behavior of magnetorheological elastomers, Smart Mater. Struct. 21 (12) (2012) 125015.
[44] M.K. Hassanzadeh-Aghdam, R. Ansari, M.J. Mahmoodi, A. Darvizeh, Effect of nanoparticle aggregation on the creep behavior of polymer nanocomposites, Compos. Sci. Technol. 162 (2018) 93–100.
[45] K. Danas, S.V. Kankanala, N. Triantafyllidis, Experiments and modeling of iron-particle-filled magnetorheological elastomers, J. Mech. Phys. Solid. 60 (1) (2012) 120–138.
[46] V. Lefevre, K. Danas, O. Lopez-Pamies, A general result for the magnetoelastic response of isotropic suspensions of iron and ferrofluid particles in rubber, with applications to spherical and cylindrical specimens, J. Mech. Phys. Solid. 107 (2017) 343–364.